VOX-STORM: A stochastic 3D model based on a dual voxel-mesh architecture for the morphological characterization of aggregates

Léo Théodon, Johan Debayle, Carole Coufort-Saudejaud

Contents lists available at ScienceDirect

Powder Technology

VOX-STORM: A stochastic 3D model based on a dual voxel-mesh architecture for the morphological characterization of aggregates

L. Théodon [a,*], J. Debayle [a], C. Coufort-Saudejaud [b]

[a] MINES Saint-Etienne, CNRS, UMR 5307 LGF, Centre SPIN, Saint-Etienne, France
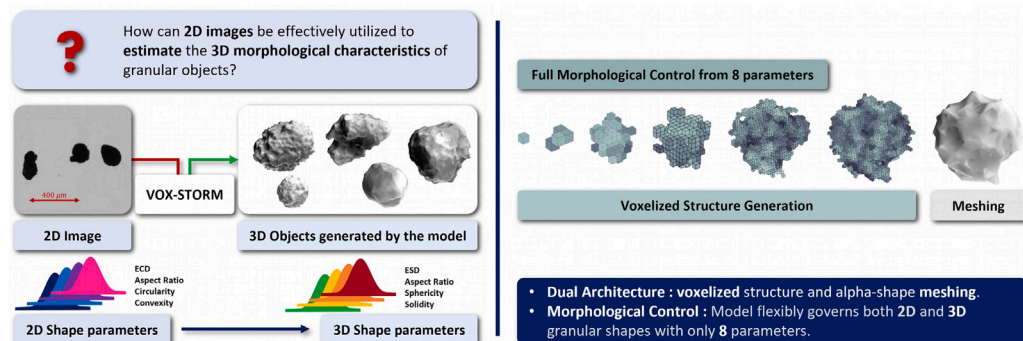[b] Laboratoire de Génie Chimique, Université de Toulouse, CNRS, INPT, UPS, Toulouse, France

GRAPHICAL ABSTRACT

HIGHLIGHTS

- VOX-STORM combines voxel structure and alpha-shape meshing.
- Generates 1000 objects in <20 s with full morphological control.
- Validated with 3D prints and 40,000 synthetic objects.
- Estimates 3D properties from 2D image measurements.
- Predictions validated with latex aggregate measurements.

ARTICLE INFO

ABSTRACT

Measuring the 3D morphological properties of granular objects such as aggregates is a critical issue in many fields of science and industry, especially when the objects are fragile or hard to sample. For these reasons, non-invasive techniques based on image analysis are being developed. However, most image analysis techniques can only measure 2D properties. This paper presents a new approach based on both image analysis and a 3D stochastic geometric model called VOX-STORM (VOXel-based STOchastic geometRical Model) to estimate 3D morphological properties. By adjusting the parameters of the model, the latter is able to generate populations of objects whose 2D property distributions match those measured by image analysis, and to predict 3D morphological property distributions. The model is based on a dual architecture combining voxelized structure and alpha-shape meshing of the external surface, which makes object generation extremely fast (about 1000 objects in 20 s), while allowing rapid computation of 3D characteristics. The method is validated twice, first on 3D printed aggregates and then on a population of 40,000 synthetic aggregates, with mean errors of less than 2.5% in all cases and less than 1% for 2D properties. It is then applied to two sets of images

* Corresponding author.
E-mail addresses: l.theodon@emse.fr (L. Théodon), debayle@emse.fr (J. Debayle), carole.saudejaud@toulouse-inp.fr (C. Coufort-Saudejaud).

of latex aggregates captured by a morphogranulometer. The morphological property distributions and fractal dimensions are compared to ground truth in the 2D case and to laser diffraction measurements in the 3D case. The results are also compared with two other recent stochastic geometric models, and the VOX-STORM model outperforms them in all scenarios, as well as in speed of execution, while agreeing with experimental measurements. Finally, directions for future work are suggested.

1. Introduction

The morphological characterization of aggregates, agglomerates and granular objects in general is a field of study with numerous applications in a wide range of scientific fields, from medicine [1] to the chemical [2], food [3,4] and civil engineering [5] industries. In fact, the morphological characteristics of these highly diverse objects - i.e., their size, shape, and texture - can have a significant impact on the physicochemical properties [6] of the materials they compose, and consequently on their structure [7], strength [8,9], taste, hazard [6], and environmental impact.

For example, Guérin et al. [10] discuss the importance of characterizing aggregate morphology when monitoring separation processes in water production or wastewater treatment. In fact, the size, shape and density of flocs formed during treatment stages affect sedimentation rates and overall process efficiency. Bower et al. [11] reports that studying the fractal characteristics of aggregates helps to analyze the behavior and properties of building materials, particularly in terms of particle interactions, settlement efficiency, and overall performance. Furthermore, according to Tang et al. [12], who is interested in the fractality of structures formed by aggregates of latex nanoparticles using image analysis, characterizing the morphology of these irregular structures provides a better understanding of the links between their structural properties and the phenomena that lead to their formation, as well as the impact of their morphology on various industrial processes and applications, such as solid–liquid separation processes.

For all these reasons, many techniques have been developed to analyze and understand the morphology and complex structure of aggregated objects. Discrete Element Method (DEM) models are particularly well suited to modeling fine multiphysics interactions between elementary particles, although they can be quite complex to implement and demanding in terms of computational power [8,9,13–15]. Population balance models are relatively efficient and easy to implement, and can quickly provide size and sometimes shape distributions [16,17]. However, they do not provide complete knowledge of the structure and morphology of objects, especially the more subtle features of angularity and texture. Thus, thanks to the increasing power of computers, techniques based mainly on image analysis have experienced rapid growth in recent years [18].

In particular, image analysis techniques based on machine learning models such as CNN (Convolutional Neural Network) or Mask R-CNN have been used in pharmaceutical applications for in-line recognition of agglomerated pellets [19] or for automatic segmentation of aggregates of titanium dioxide particles from SEM or TEM images [6,20], an application for which GANs (Generative Adversarial Networks) were also developed [21]. While these techniques are very powerful, they have a number of limitations. In fact, they require training data, which implies the ability to generate images representative of real data, often using a model that can be complex to implement if realistic rendering is required, or the ability to acquire images by SEM, TEM, or tomography in the case of 3D characterization, which is a costly and complex process [22]. In addition, the information obtained by image analysis is the result of segmentation performed on 2D images and does not capture the complex three-dimensional structure of objects [23]. Therefore, hybrid methods based on the use of models are being developed to extract 3D information from projected 2D images [24].

The main idea behind these hybrid methods, which will be explored in this paper, is based on the principles of stochastic geometry, where a model is used to generate a 3D population representative of reality by adjusting the model parameters. In the context of this work, information collected from 2D images is used to adjust the model parameters. Since the object population generated by the model is representative of real data, its 3D morphological characteristics can be measured and predictions can be made.

Many models have been developed to study aggregates. For example, Liu et al. [8] uses X-ray tomography and finite element simulation to study the influence of aggregate morphology on the mechanical behavior of bituminous mixtures. Moreaud et al. [25] proposes a stochastic model based on Boolean multiscale models for analyzing 3D images of complex materials. Another geometrical stochastic model proposed by Moreaud et al. [26] allows the fractal dimension of objects composed of large aggregate particle systems to be adjusted as a function of model parameters, as does another model proposed by Tomchuk et al. [27], where the fractal dimension is also adjustable, and which aims to characterize the structure of aggregates through spatial correlation in direct and reciprocal space, and the effect of the structure factor in small-angle scattering.

In general, there are many models for modeling aggregates that allow to adjust one (very often the fractal dimension) or more morphological features as a function of the model parameters. However, they do not allow efficient generation of object populations with the goal of matching projected 2D morphological feature distributions (area, perimeter, etc.) to target distributions, e.g. measured by image analysis. This paper develops a new model specifically for this purpose. Previous attempts had already led to the development of a model based on hard sphere packing on the one hand (GRAPE: Théodon et al. [28]), and another model based on deforming the mesh of an ellipsoid of random Gaussian fields on the other hand (SPHERE: Théodon et al. [29]). Both approaches have limitations, including performance problems with hard sphere stacking and a priori estimation of object volume, which limits the range of applications, and the inability to generate low-convex and high-angle structures for the latter, as well as complete ignorance of the internal structure of objects, since only the mesh of the outer surface is generated.

Therefore, the model proposed in this paper, called VOX-STORM (VOXel-based STOchastic geometRical Model), is based on a dual architecture. First, a voxelized structure is rapidly generated by successive convolutions, and then a mesh of the object is obtained by computing the surface of an alpha shape, a generalization of the concept of convex hull, sometimes called concave hull [30]. This combination of techniques not only allows extremely fast generation of objects (in contrast to techniques based on primary particle stacking or random mesh generation) and information about the internal structure of the object, such as porosity, but also provides detailed information about the surface of the object, allowing finer grained knowledge of texture and angularity. For additional flexibility, two 3D random Gaussian fields are used to modulate the activation probabilities of boundary voxels during their generation. This makes it possible to generate complex, possibly highly porous structures with an angularity and texture that could not be achieved with approaches based on hard sphere stacking or mesh deformation.

The following section explains how images of latex nanoparticle aggregates, on which morphological feature distributions were measured to provide ground truth, were acquired. The various morphological features used and measured in this article are then defined, and the theoretical basis for generating random Gaussian fields and calculating alpha shapes is presented. The VOX-STORM model is then defined

and examples of its implementation are presented. The influence of the model parameters on the morphological properties of objects is examined and discussed. The method for predicting the 3D feature distributions of object populations from projected 2D images is then presented. The process of fitting the model parameters by minimizing a cost function is described, and the method is then validated using images of 3D printed aggregates acquired by a morphogranulometer, as well as numerically on a population of 40,000 objects generated by the model. The method is then applied to two sets of 3500 images of latex aggregates captured by a morphogranulometer and obtained under different experimental conditions. The results and predictions of the model are presented and compared with those of two other stochastic geometrical models developed previously [28,29]. The object size and mass fractal dimension are compared with experimental laser diffraction measurements. Finally, the performance of the model is discussed, as well as its limitations, and avenues for future work are presented.

2. Methodology

2.1. Data acquisition

The experimental data used in this article are extracted from a series of experiments carried out by Hamieh et al. [31] with the aim of analyzing the morphology of Methacrylate Butadiene Styrene (MBS) latex aggregates according to different experimental protocols. The experiments were carried out in a 1 L jacketed cylindrical batch reactor using a procedure derived from a coagulation process described in an ARKEMA patent [32], which is of great interest for industrial applications. At the end of the aggregation process, images are taken using a morphogranulometer (Morphologi G3 – Malvern Panalytical), which combines an optical microscope with a CCD camera and image processing software. Two sets of 3500 images each are thus acquired for two different experimental protocols, which are described in detail in the Section 5.1.

2.2. Morphological characterization

All 2D morphological features measured on images captured by the morphogranulometer, as well as 2D and 3D morphological features measured on objects generated by the model, are listed in Table 1. The size characteristics ECD and ESD are calculated from the projected area A and volume V of the objects, respectively, and can be measured experimentally by laser diffraction (Mastersizer 3000) in the case of the ESD to provide an additional reference point.

Shape and angularity properties such as the circularity C, which expresses the similarity of a shape to a circle, where 1 is a perfect circle and 0 is a flattened object, are often used when studying latex aggregates [10,31,34] because they allow the size (area) of objects to be related to their texture (perimeter). Thus, the circularity measure gives an indication of the compactness of an object. However, because perimeter measurements are highly dependent on definition, image resolution, and noise, they are sometimes difficult to calculate accurately [35,36]. For this reason, the convexity Co, which is based solely on area measurements, may prove to be more robust and a substitute angularity measure for the circularity, although they are not interchangeable.

Regarding fractal dimensions, several definitions have been adopted. The Minkowski-Bouligand [33] or Box-Counting dimension can be estimated on 2D or 3D discretized objects by successively dividing the space into boxes of side ϵ, and the quantity $N(\epsilon)$ indicates the number of boxes needed to cover the boundary of the object. It is then defined as follows

$$D_{2,3}^{BC} = \lim_{\epsilon \to 0} \frac{\log N(\epsilon)}{1/\epsilon} \tag{1}$$

Table 1
List of morphological characteristics used in this paper. The perimeter and surface area include those of any interior voids.

Parameters	Symbol	Definition and equation
2D & 3D Parameters		
Feret Diameter max.	F_{max}	Longest caliper (Feret) length
Feret Diameter min.	F_{min}	Smallest caliper (Feret) length
2D Parameters		
Projected Area	A	Area of the object
Convex Area	A_c	Area of the convex hull
Perimeter	P	Length of the object outline
Equivalent Circle Diameter	ECD	$2 \times \sqrt{A/\pi}$
Aspect Ratio	AR	F_{min}/F_{max}
Convexity	Co	A/A_c
Circularity	C	$4\pi \times A/P^2$
3D Parameters		
Volume	V	Volume of the object
Convex Volume	V_c	Volume of the convex hull
Volume	V_p	Volume of the closed pores
Surface Area	S	Area of the object surface
Equivalent Sphere Diameter	ESD	$2 \times \sqrt[3]{3 \times V/(4\pi)}$
Solidity	SLD	V/V_c
Sphericity	Φ_S	$6\pi^2 \times V/(\sqrt{\pi S})^3$
Porosity	ϵ_{cp}	$1 - V_p/(V + V_p)$
Fractal Dimensions		
Power Law	D_2^{PL}	$A \propto F_{max}^{D_2^{PL}}$
Box-Counting	$D_{2,3}^{BC}$	see Falconer [33]
Laser scattering	D_3^{LS}	Experimental Data [31]

Another 2D fractal dimension can be calculated according to a power law that relates the area of objects to one of their characteristic lengths. It is defined by Florio et al. [37] as

$$A \propto l_c^{D_2^{PL}} \tag{2}$$

where l_c is the characteristic length of the objects. In the context of this article, the characteristic length is defined as the maximum Feret diameter F_{max}, which gives the definition shown in Table 1.

The last fractal dimension used is the mass fractal dimension. It is obtained by laser scattering described by Soos et al. [38] and Sorensen [39] and is a function of the scattering intensity $I(k)$, where k is the wave vector. It is defined in the fractal regime (i.e. for $R_g^{-1} \ll k \ll r_0^{-1}$ with R_g the radius of gyration of the object and r_0 the radius of the primary particles) as follows

$$I(k) \propto k^{-D_3^{LS}} \tag{3}$$

In the next section, the VOX-STORM model is presented, along with the theoretical concepts required for its implementation.

3. The proposed model: VOX-STORM

The proposed model introduces an original approach to generate 3D objects by assembling voxels, followed by the generation of a mesh using alpha shapes. The core of the method is the voxelization process, where an object is constructed by selectively activating voxels within a predefined grid. The idea is to draw inspiration from the way aggregates form, with primary particles gradually adhering to the object's boundary in numbers that depend not only on their concentration in the medium, but also on numerous other environmental and operational parameters.

The algorithm begins by setting a central voxel as the initial active point in a three-dimensional grid. It then proceeds iteratively, using a convolution kernel to evaluate the surrounding space for candidate voxel for activation. This kernel, which is designed to reflect the geometrical properties and spatial distribution desired in the final object, guides the growth of the structure by determining candidate voxels for activation at each iteration.
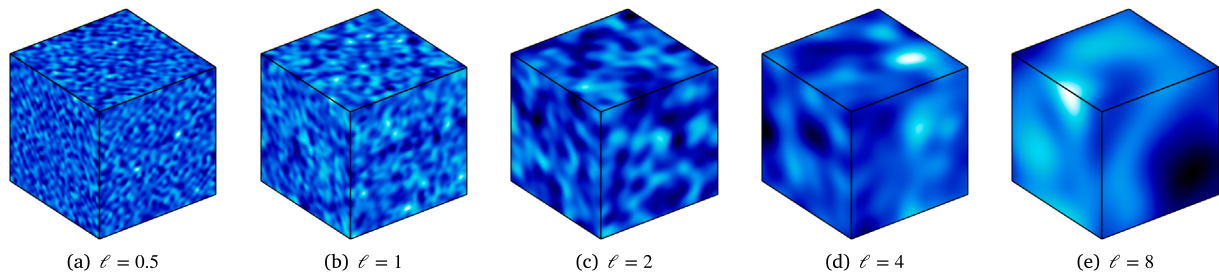
(a) $\ell = 0.5$ (b) $\ell = 1$ (c) $\ell = 2$ (d) $\ell = 4$ (e) $\ell = 8$

Fig. 1. 3D Gaussian random fields generated on a 64^3 voxel grid, showing the effect of different correlation lengths ℓ. The covariance function used is defined by Eq. (4). The color gradient from dark blue (value = 0) to bright white (value = 1) indicates the field intensity.
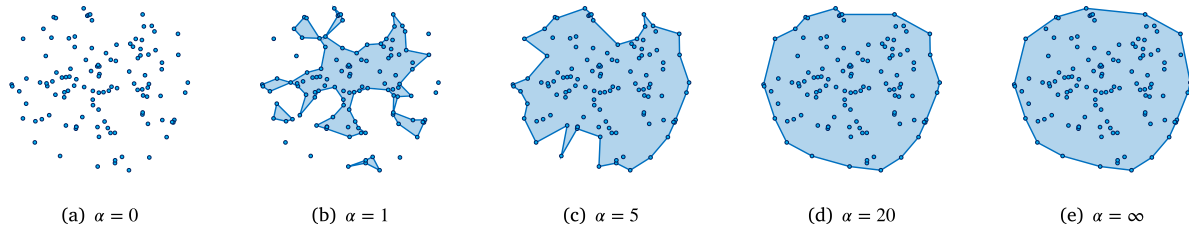

(a) $\alpha = 0$ (b) $\alpha = 1$ (c) $\alpha = 5$ (d) $\alpha = 20$ (e) $\alpha = \infty$

Fig. 2. Displaying the contours of the alpha shape of a point cloud from $\alpha = 0$, giving the point set, to $\alpha = \infty$, giving the convex hull.

The likelihood of activation of a voxel is influenced by two random Gaussian fields that simulate environmental factors or material properties that affect the growth of the object for greater control over its angularity and texture, as well as its potential porosity.

Because of its high degree of flexibility, the model can generate complex and varied structures that closely mimic natural processes. After voxelization, the model uses alpha shapes to extract a precise, continuous boundary from the voxelized object. This boundary is then used to generate a mesh. The use of alpha shapes allows the resolution and detail of the mesh to be adjusted, providing flexibility in modeling the morphological features of the object.

In this section, the theoretical tools needed to build the model (random Gaussian fields, alpha-shape) are presented. The algorithm that allows the model to generate random objects is then detailed, and examples of generated objects are shown. Finally, the influence of the model parameters on the morphological properties of the objects is analyzed and discussed.

3.1. Random Gaussian fields

The generation of a 3D Gaussian random field efficiently utilizes the approach of Adler et al. [40] and Liang et al. [41], who defined the field by convolution of uncorrelated Gaussian noise with a symmetric, normalized weight function. According to Lang and Potthoff [42], using the Fourier space for this convolution significantly increases computational speed with minimal error. This method has already been used to generate random Gaussian fields to control the morphological properties of granular objects [29].

The FFT-based generation process is outlined as follows:

1. Definition of the covariance function $\mathrm{Cov}(\vec{r})$ with an exponential-quadratic kernel or RBF kernel:

$$\mathrm{Cov}(\vec{r}) = \exp\left(\frac{-\|\vec{r}\|^2}{2\ell^2}\right), \tag{4}$$

   where $\vec{r} = (x, y, z) \in \mathbb{R}^3$ and ℓ denotes the *correlation length*.
2. Obtain the spectral power function $\widehat{\mathrm{Cov}}(\vec{k})$ as the Fourier transform of $\mathrm{Cov}(\vec{r})$:

$$\widehat{\mathrm{Cov}}(\vec{k}) = FFT\left(\mathrm{Cov}(\vec{r})\right). \tag{5}$$

3. Generate the Gaussian random field $G(\vec{r})$ as follows:

$$G(\vec{r}) = FFT^{-1}\left[\sqrt{\widehat{\mathrm{Cov}}(\vec{k})} \cdot \widehat{\mathcal{N}}(\vec{k})\right] \tag{6}$$

   where $\mathcal{N}(\vec{r})$ is an uncorrelated Gaussian noise of mean zero and variance one.

This FFT-based method enables fast 3D Gaussian random field generation. On modern computer hardware, such as an Intel(R) Core(TM) i9-12900KF with 64 GB RAM and MATLAB® (2023b), a 128^3 voxel field can be generated in about 10^{-1} s. Fig. 1 shows how the correlation length ℓ affects the structure of a random Gaussian field.

3.2. Alpha shapes

Alpha shapes are a generalization of the convex hull concept. They allow a more detailed description of the contour of a point cloud. The concept, introduced by Edelsbrunner et al. [30], relies on a parameter α to balance the granularity of the shape and its approximation to the convex hull of the point set.

The procedure for generating an alpha shape can be summarized in three steps:

1. Compute the Delaunay triangulation for the given set of points.
2. For a given α, identify all simplices (vertices, edges, triangles, etc.) in the triangulation that satisfy the α radius condition. A simplex is included if its circumcircle (in 2D) or circumsphere (in 3D) has a radius less than or equal to α.
3. The alpha shape is formed by the union of these selected simplices. As α varies from 0 to ∞, the alpha shape transitions from the point set itself to its convex hull.

The choice of α allows for flexibility in modeling the complexity of the boundary. Therefore, in the context of this work, considering a mesh drawn from the alpha shape rather than the voxellized shape of the object allows better control over its morphological properties. Fig. 2 illustrates the effect of the α parameter on the alpha shape contour of a point cloud.
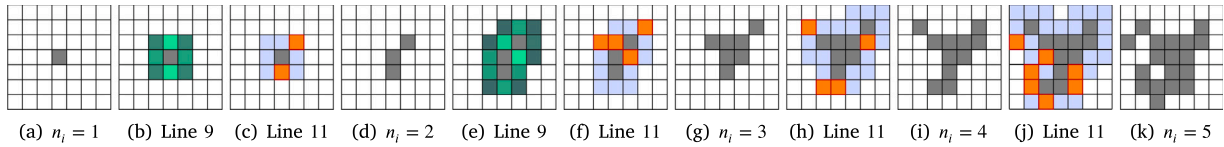
(a) $n_i = 1$ (b) Line 9 (c) Line 11 (d) $n_i = 2$ (e) Line 9 (f) Line 11 (g) $n_i = 3$ (h) Line 11 (i) $n_i = 4$ (j) Line 11 (k) $n_i = 5$

Fig. 3. 2D visualization of Algorithm 1 applied to a 7×7 grid, with parameters $\lambda = 0.3$ and $w = 2$. (a) shows the initialization phase; (b) illustrates the calculation of activation probabilities at the boundary, with lighter shades indicating higher probabilities; (c) shows the random selection of pixels for activation. The following figures (d-k) show the growth of the 2D shape. Legends show number of iterations and corresponding lines in Algorithm 1.
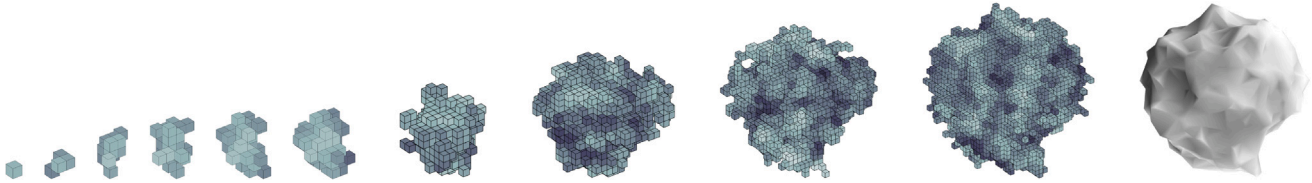

Fig. 4. Illustration of object construction by the model on a 49^3-voxel grid with $\lambda = 0.15$. The state of the grid is shown for iterations 1 to 5, and then for iterations 10, 20, 30, and 40, from left to right. The final object, including the mesh derived from the surface of an alpha shape (with $\alpha = 5$), is shown on the far right. The color gradient on the voxelized structures indicates the intensity of the random Gaussian field product, going from darker (value = 0) to lighter (value = 1).
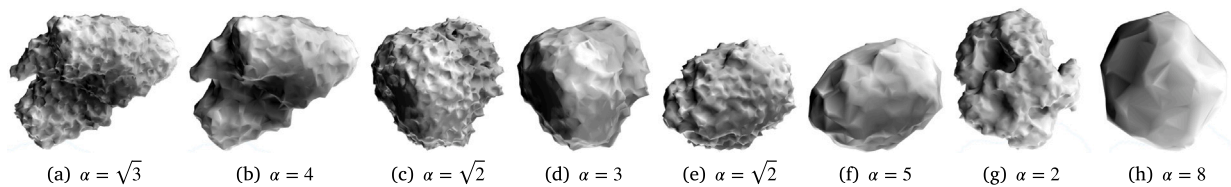

(a) $\alpha = \sqrt{3}$ (b) $\alpha = 4$ (c) $\alpha = \sqrt{2}$ (d) $\alpha = 3$ (e) $\alpha = \sqrt{2}$ (f) $\alpha = 5$ (g) $\alpha = 2$ (h) $\alpha = 8$

Fig. 5. Examples of objects generated by the VOX-STORM model with different parameter sets, showing meshes calculated with two different α values to illustrate the effect of the parameter on the object texture.

Algorithm 1 Voxel-based random structure generation

1: Initialize W to size $n_g \times n_g \times n_g$ and value 0
2: Set the central voxel of W to 1 (activation)
3: Define the convolution kernel on a $3 \times 3 \times 3$ volume

$$K_w(x, y, z) = c \times \exp\left(-\frac{1}{2}\left(\frac{x^2}{w^2} + y^2 + z^2\right)\right)$$

where c is a normalization constant.
4: Compute the random Gaussian fields G_A and G_T
5: $G \leftarrow G_A^{c_A} \cdot G_T^{c_T}$
6: **for** $k = 1$ to n_i **do**
7:     $B \leftarrow \text{convolve}(W, K_w)$
8:     $B \leftarrow B \cdot (1 - W_{\texttt{filled}})$
9:     For each voxel v in B, calculate the activation probability $P_{\text{act}}(v)$ as:

$$P_{\text{act}}(v) = \frac{B(v) \times G(v)}{\sum_x B(x) \times G(x)}$$

10:     Compute the number n_a of pixels to activate with

$$n_a = \text{Poisson}\left(\lceil \lambda \times \text{card}(B)\rceil\right).$$

11:     Draw without replacement from P_{act} and activate n_a voxels in W.
12: **end for**

3.3. Model description

The procedure for generating a 3D object using the VOX-STORM model includes two main steps: generating the voxel-based structure using a stochastic process and generating the mesh using alpha shapes. The method for generating the voxel-based structure of the object is described in Algorithm 1. It is an iterative process in which the number of voxels is increased by successive activation at the boundary. The main points are as follows:

1. An empty W grid of size n_g^3 is initialized to 0 and the central voxel is activated (set to 1).
2. A Gaussian kernel K_w is defined, with the w parameter controlling the elongation of the object.
3. Two random Gaussian fields G_A and G_T with respective correlation lengths ℓ_A and ℓ_T are generated. They are raised to the power of c_A and c_T, respectively, to modify their intensity. In particular, they are used to control the angularity (G_A) and texture (G_T) of the object.
4. Each iteration repeats the following steps.

   - The extended boundary B of W is computed using the convolution kernel K_w.
   - (*Optional*) The grid $W_{\texttt{filled}}$ is calculated by performing a morphological hole-filling operation [43] on the grid W to account for porosity.
   - The elements of $W_{\texttt{filled}}$ (or W) are removed from the extended boundary B.
   - The activation probability density function P_{act} is calculated and modulated by the random Gaussian fields.
   - A number n_a of voxels are activated according to the distribution P_{act}. This number depends on a Poisson distribution whose intensity is proportional to the cardinality of B and a parameter λ.

5. The alpha shape S_α of the voxelized structure contained in W is computed and the mesh of the object is defined as the boundary of S_α.

(a) n_i vs. ESD   (b) c_A vs. SLD   (c) c_A vs. Φ (d) α vs. SLD and α vs. Φ

Fig. 6. Influence of the model parameters on the 2D morphological characteristics of the generated objects. Each observation represents an average measured over a sample of 500 objects, and standard deviations are displayed.

(a) n_i vs. ESD   (b) c_A vs. SLD   (c) c_A vs. Φ (d) α vs. SLD and α vs. Φ
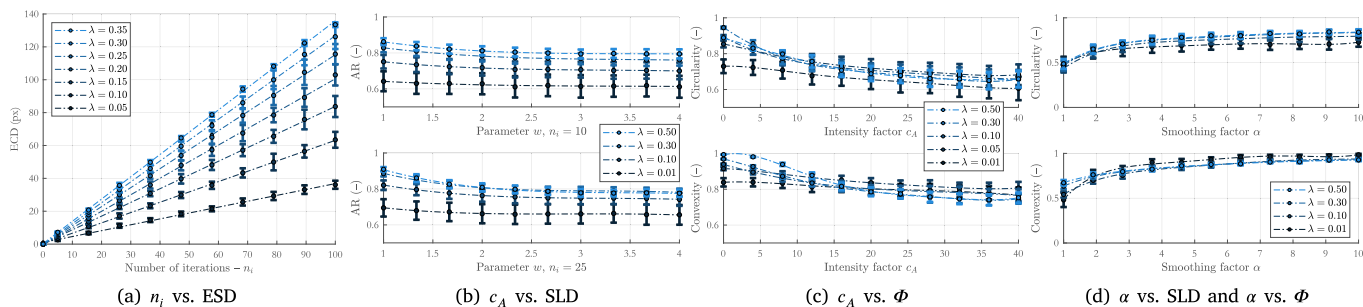
Fig. 7. Influence of the model parameters on the 3D morphological characteristics of the generated objects. Each observation represents an average measured over a sample of 500 objects, and standard deviations are displayed.
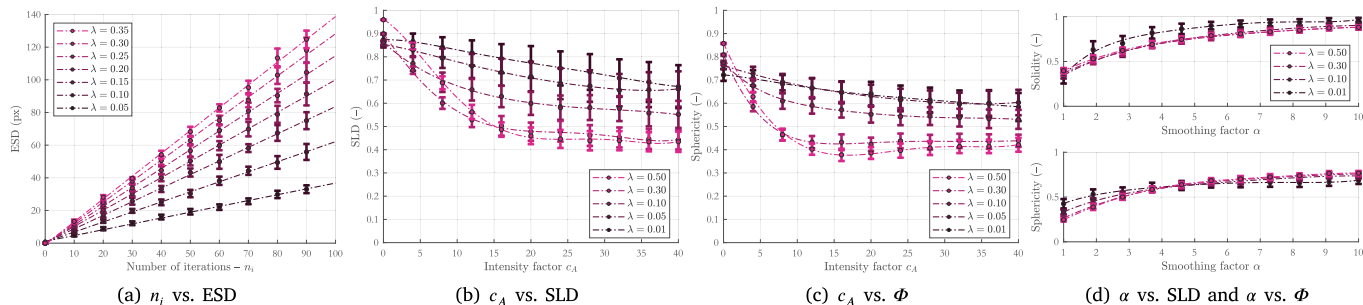
Table 2
List of the 8 base parameters of the proposed model.

Parameter	Interval	Definition
n_i	$[0;+\infty[$	Number of iterations
λ	$]0;1]$	Proportion of voxels to activate in B
w	$[0;+\infty[$	Weight for the convolution kernel K_w
α	$[\sqrt{2};+\infty[$	Smoothing of the alpha shape
ℓ_A	$[0;+\infty[$	Correlation length of the random field G_A
ℓ_T	$[0;+\infty[$	Correlation length of the random field G_T
c_A	$[0;+\infty[$	Intensity factor of G_A
c_T	$[0;+\infty[$	Intensity factor of G_T

Table 3
Main influence of model parameters on the morphological properties of the objects.

Parameter	Impact	Properties
n_i	Size	ECD, ESD, …
w	Shape	AR, C, Phi
ℓ_A, c_A	Shape and Angularity	AR, C, Co, SLD, Φ
ℓ_T, c_T	Angularity and Texture	C, Co, SLD, Φ
α	Angularity and Texture	C, Co, SLD, Φ
λ	All Properties	–

In this form, the model depends on 8 parameters, which are listed in Table 2 and whose influence on the morphological properties of the objects will be discussed in the following section. There is only one meta parameter, namely the size n_g of the W grid, which also defines the size of the 3D domains on which the random Gaussian fields are defined. Fig. 3 illustrates the process of creating a 2D object in the case of a 7×7 grid, with the formation of a closed pore (Fig. 3(k)) after 4 iterations and Fig. 4 shows the evolution of the voxelized 3D structure at each iteration, as well as the final result obtained by computing the alpha shape contour.

Fig. 5 shows several examples of objects generated by the VOX-STORM model based on different parameter sets. Each object is shown with two different α values to illustrate qualitatively the effect of this parameter on the surface texture without changing the overall shape of the object. In particular, the flexibility of the model allows it to generate objects that are concave (Figs. 5(a) and 5(b)), compact (Fig. 5(f)), or rather porous (Fig. 5(g)).

3.4. Impact of the parameters

In this section, the influence of the model parameters on the 2D and 3D morphological features of the objects is studied. Understanding how each parameter affects object shape and structure is key to simplifying

the optimization process. This allows to determine which settings best achieve the desired morphological distributions. Table 3 summarizes the impact of each model parameter on the morphological properties of the generated objects, while Figs. 6 and 7 provide quantitative insights into how these aspects vary with parameter settings.

Number of iterations – n_i

For a fixed intensity λ, the number of iterations n_i is strongly correlated with the size of the object, with a linear relationship with the ECD (Fig. 6(a)) and the ESD (Fig. 7(a)). This property is easily understandable in 3D for the ESD due to the object generation process, where the volume grows on average in proportion to the surface area and λ at each iteration n_i, but less so in 2D for the ECD. In reality, this linear relationship between the ECD and n_i is only really visible when the 2D projection of the object is viewed in a direction orthogonal to the maximum Feret diameter, as is the case for the results shown in Fig. 6(a). To obtain these results, 500 objects were generated per observation. The remaining parameters were chosen randomly using uniform laws.

In terms of optimization, the fact that object size is linearly correlated with the number of iterations means that the ECD measurements taken on 2D projection images can be used as input to the model with respect to n_i.

Weight for the convolution kernel – w

The only purpose of the weight w associated with the convolution kernel K_w is to slightly adjust the aspect ratio (AR) of the object. Fig. 6(b) shows that this parameter has a small effect on the final shape of the object (on the order of 5% to 10%), but is still significant. These data were obtained with a constant α parameter and with random Gaussian fields disabled.

Furthermore, in the case where $w = 1$, it can be seen that the intensity parameter λ has a strong influence on AR. It can also be seen that lower intensities λ and fewer iterations n_i result in more elongated objects on average, while higher intensities and more iterations result in larger and rounder objects.

Random Gaussian fields – $G_A \& G_T$

The Gaussian random fields G_A and G_T are mainly used to modify the angularity and texture of the objects, although G_A also has a non-negligible effect on their shape (AR) for high intensities c_A. Fig. 6(c) shows the effect of a single random field (G_A) on the circularity and convexity as a function of the intensity c_A, with the second random field disabled, for $w = 1$ and the parameter α held constant. The effect on the 3D counterpart of these morphological features is illustrated in Fig. 7(b) for the solidity and Fig. 7(c) for the sphericity.

In general, a combination of two Gaussian random fields with different correlation lengths $\ell_A > \ell_T$ and different intensities c_A and c_T allows fine control over the 3D morphological properties of the generated objects. For example, the concave object in Fig. 5(a) is generated with a random field G_A of high intensity c_A, as is the porous structure of the object in Fig. 5(g). The bumpy texture of Fig. 5(e), on the other hand, is only possible with the correct parameterization of the random field G_T.

Smoothing factor – α

The parameter α is directly related to the alpha shape from which the mesh of the object is extracted. Thus, its influence on the texture and angularity of the object is considerable, while its influence on the size and shape of the object is minimal (see Fig. 5). Its effect on the morphological properties of angularity and texture in 2D (C and Co) and 3D (Φ and SLD) is illustrated in Figs. 6(d) and 7(d), respectively.

Intensity – λ

The intensity factor λ affects all the size, shape, angularity, and texture properties of the object generated by the model, as shown in Figs. 6 and 7. This phenomenon is similar to that observed in the agglomeration process of latex nanoparticles under hydrodynamic constraints, for example, where the morphology of the aggregates strongly depends on the concentration of elementary particles in the medium [31], although no direct relationship can be established between the parameters of the geometrical model VOX-STORM and the operational parameters.

An important point to note is that there is a strong correlation between the quantity $n_i \times \lambda^{2/3}$ and the ECD – when objects are observed in a direction orthogonal to the maximum Feret diameter – on the one hand, and the ESD on the other hand, as shown in Figs. 8(a) and 8(b), respectively. Indeed, the linear regression models below can be established:

$$\widehat{\text{ECD}} = 1.38 n_i \times \lambda^{2/3} + 2.75 \tag{7}$$

and

$$\widehat{\text{ESD}} = 2.56 n_i \times \lambda^{2/3} + 0.78 \tag{8}$$

where $\widehat{\text{ECD}}$ and $\widehat{\text{ESD}}$ are the estimators of ECD and ESD, respectively, and the adjusted coefficients of determination $\bar{R}^2$ given by the exact Olkin-Pratt estimator [44] and shown in Fig. 8 are $\bar{R}^2 = 0.988$ for the ECD and $\bar{R}^2 = 0.989$ for the ESD.

Thus, as mentioned above, this strong correlation between n_i, λ and the ECD or the ESD not only allows the direct use of data obtained by image analysis to simplify the optimization process, but also provides precise knowledge of particle size distributions (PSD) in number and volume in relation to the model parameters.
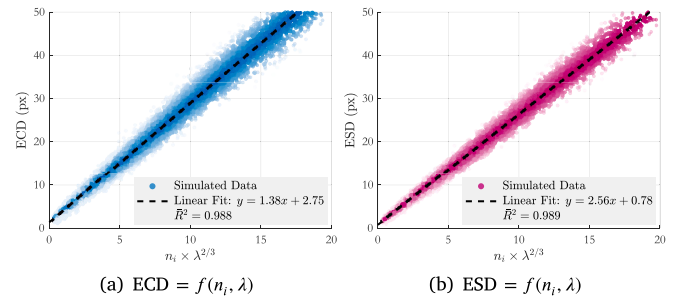

(a) ECD $= f(n_i, \lambda)$ (b) ESD $= f(n_i, \lambda)$

Fig. 8. Correlation of the product $n_i \times \lambda^{2/3}$ with the ECD (a) and the ESD (b).

3.5. Discussion

From its speed and flexibility to the high degree of control provided by the various parameters, the proposed model is unique in many respects.

- *Speed*: The model is capable of generating 1,000 objects similar to those shown in Fig. 5 in about 20 seconds. This is of the same order of magnitude as other methods that propose to generate the mesh of granular objects from random Gaussian fields [29,45], although limited to star-shaped objects, and superior to other methods based on surface subdivisions [46]. Other methods with similar speeds exist [47,48], but do not allow fine control of object angularity or texture. However, these methods only generate a mesh without providing any information about the internal structure of the objects. In addition, the shapes are typically not very complex, and control over angularity, texture, porosity, or concavity is limited or nonexistent. Other methods based on stacks of hard spheres exist [28], but are generally at least an order of magnitude slower [28], or less suitable for generating granular and/or compact objects [49,50], or both.

- *Morphological Control & Flexibility*: With a relatively small number of parameters, the model is capable of generating objects with widely varying morphological characteristics while maintaining a high degree of control. Alpha shapes allow the modulation of angularity and texture in objects, with subtle changes in shape and minimal changes in size, even though these changes are measurable. The duality between mesh and voxel structure allows fine measurement of properties such as surface area or perimeter (and thus circularity and sphericity), which are usually difficult to calculate on discretized objects [35], while providing accurate knowledge of the internal structure of objects, particularly porosity. Meanwhile, equivalent methods based on mesh generation generally offer much less control or flexibility over object angularity and texture [46–48,51], or depend on a very large number of parameters [52]. Moreover, although the objects studied in this article are rather isotropic, it is quite possible to generate non-isotropic aggregates by adjusting the shape parameter w, choosing a completely different and anisotropic convolution kernel, or even considering the use of non-isotropic random fields for G_A and G_T. The convolution kernel was chosen empirically because of its ease of implementation and the fact that it is sometimes possible to establish relationships between its parameters and the properties of the objects generated by the model [53]. However, several other types of kernels have been tested, and this choice can have a significant impact on the overall morphology, especially at low iteration counts.

- *PSD Integration*: Due to the linear dependency between object size and number of iterations n_i, a size density (2D or 3D) can be entered directly into the model, allowing for easy generation of calibrated object populations. As a result, the number of parameters to adjust is reduced and the optimization process can focus on the morphological features of shape, angularity, and texture.
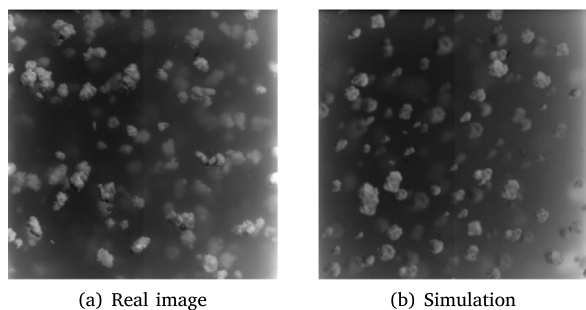
(a) Real image   (b) Simulation

Fig. 9. Comparison between an in-situ image of latex nanoparticle agglomeration in a stirred tank (a) and a 3D rendering using the VOX-STORM model (b). The model independently generated aggregates that were randomly placed in a uniform distribution to create a pseudo-3D effect.

- *Rendering Capability*: An auxiliary benefit of the model is its ability to rapidly generate photorealistically rendered objects with full knowledge of their 2D and 3D morphological features and internal structure (Fig. 9). This can be extremely useful when designing training databases for machine learning or deep learning applications.

Overall, the VOX-STORM model allows for extremely fast generation of granular objects with great control over morphological properties such as size, shape, angularity, and texture. A key feature is the use of alpha shape in addition to voxel structure. The objects are generated at least as fast as with mesh deformation models, but with much more flexibility.

The main limitation of the model is that, as with any iterative process, the computation time increases with the size of the object to be generated. Nevertheless, Fig. 5 shows that it is possible to generate sufficiently detailed high-resolution objects quite efficiently.

4. Optimization & validation

This section describes how to adjust the parameters of the model to generate objects whose 2D morphological features match those obtained by image analysis. The key concept is that distributions of 2D morphological features (such as ECD, circularity, and convexity) can be accurately measured using image analysis techniques on sufficiently large datasets to be representative. The datasets examined in this article consist of 3500 images each, with a range of 5000 to 15,000 objects per dataset. After obtaining these distributions, a cost function is defined to measure the discrepancy between the feature distributions of the model-generated objects and those derived from image analysis. The optimal parameterization of the model is then achieved by minimizing this cost function.

4.1. Optimization process

Given two morphological feature distributions, a quick and easy way to compare them is to use the method of moments. Although there are other techniques for comparing two distributions or two samples [54], the method of moments offers the advantage of being easy to implement, particularly fast in terms of computational time – an important point in the context of an optimization process – and has proven to be quite effective in the case of this work.

Given a set of parameters Ω, a cost function $F_{\text{cost}}(\Omega)$ is defined based on the Mean Relative Error (MRE) over the moments of four distributions: Equivalent Circular Diameter (ECD), Aspect Ratio (AR), Circularity (C), and Convexity (Co). The cost function aggregates the MRE of the first two moments of these distributions, each weighted

appropriately to reflect their relative importance in the performance of the model.

$$F_{\text{cost}}(\Omega) = \sum_{i=1}^{2} (\ v_i^{\text{ECD}} \cdot \delta_i^{\text{ECD}}(\Omega) + v_i^{\text{AR}} \cdot \delta_i^{\text{AR}}(\Omega) \tag{9}$$
$$+ v_i^{\text{C}} \cdot \delta_i^{\text{C}}(\Omega) + v_i^{\text{Co}}(\Omega) \cdot \delta_i^{\text{Co}})$$

Where:

- $v_i^{\text{ECD}}, v_i^{\text{AR}}, v_i^{\text{C}},$ and v_i^{Co} are the weights assigned empirically to the first and second moments of the ECD, AR, C, and Co distributions, respectively.
- $\delta_i^{\text{ECD}}(\Omega), \delta_i^{\text{AR}}(\Omega), \delta_i^{\text{C}}(\Omega),$ and $\delta_i^{\text{Co}}(\Omega)$ denote the MRE of the first and second moments for the respective distributions measured by image analysis on the one hand, and those of the objects generated by the model using the parameter set Ω on the other hand.

The cost function is then optimized using Particle Swarm Optimization (PSO) [55], an algorithm well suited to stochastic processes and proven effective in similar applications [29,56], to determine the optimal parameter set. Regarding the choice of weights, a heuristic has emerged suggesting that decreasing weights according to the granularity of the morphological feature description – size, shape, angularity, texture – tends to perform well. For example, weights such as 8 for the means of Equivalent Circular Diameter (ECD), 4 for Aspect Ratio (AR), and 2 for Circularity (C) and Convexity (Co), with a similar distribution of standard deviations (4, 2, 1, and 1, respectively), have been used.

4.2. Validation

4.2.1. On 3D printed aggregates

To ensure that the model parameters derived from the optimization process can be adjusted to produce objects that are representative of the real data, synthetic aggregates are created using additive 3D printing and then imaged using a morphogranulometer (Morphologi G3 – Malvern Panalytical). The approach is to use 2D measurements from these images to adjust the parameters of the model. This allows the predictions of VOX-STORM at both the 2D and 3D levels to be compared to the ground truth known from the reference STL file containing the mesh used in the 3D printing process.

The following method is used:

1. Approximately one thousand aggregates, each about 2 mm long, are 3D printed from a reference STL file representing a blackberry (Fig. 10(a)).
2. A set of 1,000 images of 3D printed objects are captured using a morphogranulometer (Fig. 10(b)) and then binarized (Fig. 10(c)). It is assumed that the objects are observed in a direction orthogonal to the maximum Feret diameter, with the objects naturally orienting themselves in a preferred direction under the effect of gravity.
3. Measurements of 2D morphological features are performed on the binary images to construct the cost function F_{cost} as shown in Eq. (9). In this specific context, second moments (standard deviation) are not considered because the objects are almost identical in all instances, with variations in morphological characteristics due to the manufacturing process measuring at most 2.5% on average.
4. The cost function F_{cost}, based on average values from 512 aggregates, is minimized by Particle Swarm Optimization with a runtime of approximately 1 h and an optimal parameter set Ω_0 is found.
5. A set of 512 synthetic objects is generated by the VOX-STORM model (Fig. 10(e)) with the optimal parameter set Ω_0, and morphological feature measurements are performed on 2D projections (Fig. 10(d)) made in a direction orthogonal to the maximum Feret diameter. The results are presented in Table 4.
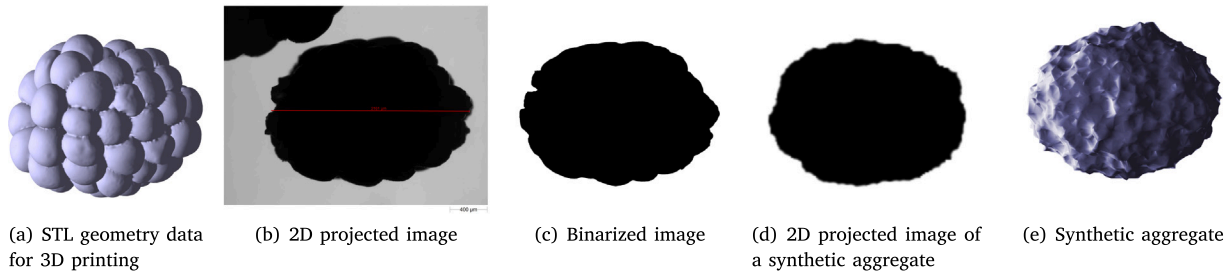
(a) STL geometry data for 3D printing   (b) 2D projected image   (c) Binarized image   (d) 2D projected image of a synthetic aggregate   (e) Synthetic aggregate

Fig. 10. Illustration of the process of generating real data from calibrated 3D printed aggregates by generating images using a morphogranulometer, and comparison with a synthetic aggregate generated by VOX-STORM.

Table 4
Comparison between 2D and 3D characteristics of 3D printed aggregates (ground truth) and synthetic aggregates generated by the proposed model with the optimal set of parameters. The values shown for synthetic aggregates are averages calculated from a set of 512 aggregates. Values are rounded to the nearest two decimal places.

	2D						3D					
Characteristics	A (mm^2)	A_c (mm^2)	P (mm)	AR	Co	C	V (mm^3)	V_c (mm^3)	S (mm^2)	ESD (mm)	SLD	Φ_S
Ground Truth	2.73	2.86	6.75	0.71	0.95	0.75	2.34	2.76	11.25	1.65	0.84	0.66
VOX-STORM	2.71	2.85	6.77	0.72	0.95	0.74	2.35	2.80	11.09	1.65	0.84	0.68
Relative Error (%)	0.58%	0.51%	0.25%	0.62%	0.40%	0.69%	0.43%	1.50%	1.41%	0.03%	0.13%	2.5%

Table 5
Specification of the parameter set Ω_s, utilized for generating a population of 40,000 synthetic aggregates, alongside the estimated parameter set $\widehat{\Omega}s$, derived from the optimization process aimed at minimizing the cost function F_{cost}.

Parameters	n_i	w	ℓ_A	c_A	ℓ_T	c_T	α	λ
Ω_s	From Eq. (10)	5	10	5	0.5	1.5	3	0.050
$\widehat{\Omega}_s$	From Eq. (7)	5.2	9.68	4.77	0.56	1.61	3.02	0.052

The results for relative errors of 2D and 3D feature averages are very good, with relative errors all below 1% for 2D features and below 2.5% for 3D features. In particular, these results validate the ability of the model to correctly predict object morphological features from projected 2D images in the case where the observed object is rather convex, has some cylindrical symmetry, and the projection is made in a direction orthogonal to the maximum Feret diameter.

However, models that use either hard sphere stacking [28] or mesh deformation [29] give comparable results. The first approach tends to take a little more time, while the second proves to be a slightly faster. Therefore, in order to facilitate a direct comparison of VOX-STORM with other state-of-the-art models, the following section will apply this method to two different populations of latex aggregates.

In addition, it is important to note that while the stochastic geometry approach may yield favorable results in terms of average morphological measurements, it is not well suited for accurate one-to-one reconstruction of 3D objects. The approach really excels at generating populations of objects that are representative of the diversity observed in real-world scenarios.

4.2.2. On a population of synthetic objects
In the previous section, the optimization process was validated on a population of quasi-identical 3D printed objects. Thus, in this section, a population of 40,000 aggregates is generated by the VOX-STORM model from a set of parameters Ω_s detailed in Table 5. In order to generate objects of different size and morphology, the number of iterations n_i, which is directly related to the size of the aggregates (Eqs. (7) and (8)), is a random variable depending on a beta law as follows:

$$n_i \sim 5 + \lceil 150 \times \text{Beta}(a, b) \rceil, \quad a = 3 \quad \text{and} \quad b = 25. \tag{10}$$

To simulate the conditions under which images are captured by a morphogranulometer, 2D projected images are generated in a direction orthogonal to the maximum Feret diameter. Subsequently, 2D

morphological features related to size, shape, and texture are measured (Fig. 11). The moments of the obtained distributions are used to construct a cost function (Eq. (9)), applied to populations of 2048 aggregates, which is then minimized by Particle Swarm Optimization (PSO) with a runtime of approximately 4 h to derive an estimator for the optimal parameterization, $\widehat{\Omega}_s$.

Table 5 shows that the differences between the parameter set Ω_s and its estimator $\widehat{\Omega}_s$ are minimal, and the 2D and 3D morphological feature distributions obtained from the optimization process are very close to the ground truth (Fig. 11). Furthermore, it should be noted that the estimated number of iterations, $\hat{n}_i$, is derived as a random variable from the distribution of the ECD measured on the projected 2D images by inverting the linear relationship outlined in Eq. (7).

Finally, Table 6 shows the statistical distance [57] - or Total Variation Distance - between the morphological feature distributions of the objects generated by the set of parameters Ω_s and their estimates. The Total Variation Distance is a simple quantitative measure for quantifying the distance between two distributions, ranging from 0 (identical distributions) to 1 (completely different distributions), and is defined as follows

$$TV(p, q) = \frac{1}{2} \int_{-\infty}^{+\infty} |p(x) - q(x)| dx \tag{11}$$

where p and q are two probability density functions.

The low Total Variation Distance values presented in Table 5 further confirm the validity of the method to estimate the morphological characteristics of an object population by analyzing 2D projected images and minimizing the cost function defined by Eq. (9). Therefore, in the following section, the proposed method is used to estimate the 2D and 3D morphological characteristics of two populations of latex nanoparticle aggregates whose images are captured by a morphogranulometer.

5. Application

5.1. Method description

This section examines images taken from two different series of aggregation experiments performed by Hamieh et al. [31] to study the morphological evolution of MBS latex particles under varying physicochemical conditions. The first series (Exp. 1) used a stirring speed of 200 rpm with a coagulant concentration of 4.16 mmol/L at destabilization temperatures of 30 °C, resulting in the formation of smaller, less
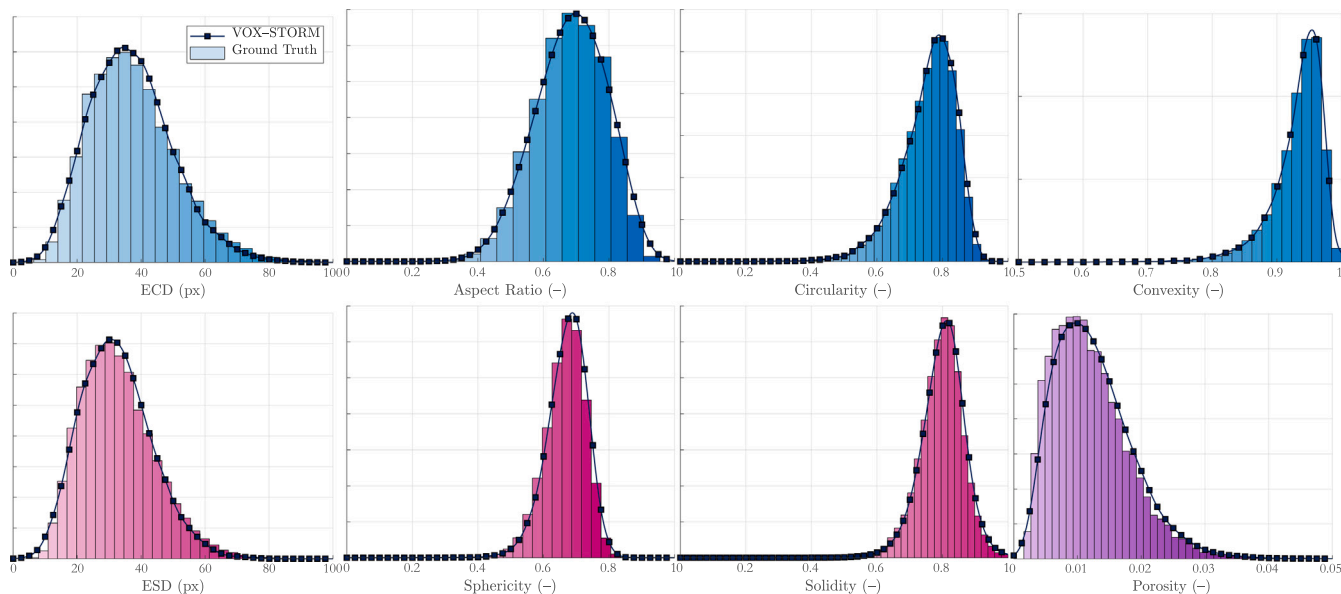
Fig. 11. Comparison of the 2D and 3D morphological characteristics between two populations generated by the VOX-STORM model: one consisting of 40,000 objects using the set of parameters Ω_s (ground truth, represented by histograms) and the other comprising 20,000 objects generated with the set of parameters $\widehat{\Omega}_s$, as estimated by the optimization process (depicted with solid lines).
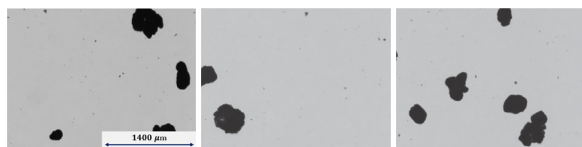
Table 6
Total Variation Distance between the morphological feature distributions (Fig. 11) of the population of objects generated from the parameter set Ω_s and the population generated from the estimated parameter set $\widehat{\Omega}_s$.

Characteristics	2D				3D			
	ECD	AR	Co	C	ESD	SLD	Φ	ε_{cp}
Total Variation Distance	0.032	0.018	0.016	0.022	0.033	0.030	0.037	0.040
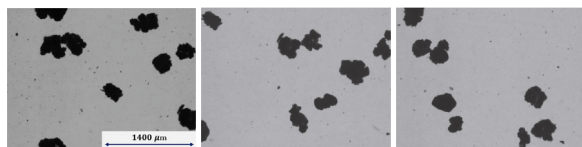
(a) Images from Exp. 1

(b) Images from Exp. 2

Fig. 12. Example of images captured by the morphogranulometer for experiments Exp. 1 and Exp. 2. The width of each image is 2.8 mm for 2584 px.

compact aggregates. The second series (Exp. 2) uses the same stirring speed of 200 rpm and a coagulant concentration of 2.08 mmol/L, with a higher destabilization temperature of 42 °C, resulting in larger, more densely packed aggregates. Fig. 12 shows examples of the images obtained by the granulometer at the end of each of these experiments, i.e. after heating the solution to a temperature of 95 °C in both cases. The aggregates from Exp. 1 appear smaller in size and lower in density, properties that can be explained by the higher acid concentration and lower destabilization temperature.

The main objective of this section is to apply the previously described and validated method to the two sets of 3500 images from each of the two experiments. This means that the parameters of the VOX-STORM model will be optimized in order to find two optimal parameterizations that match the 2D morphological feature distributions

of the objects generated by the model with the distributions measured on the images captured by the morphogranulometer. In addition, once the model parameters have been adjusted, it should also be able to predict the 3D morphological feature distributions of the observed objects. Since the ground truth in terms of 3D morphological feature distributions is unknown, the predictions of the model are compared with those of two other different recently published stochastic geometrical models.

- SPHERE [29]: a 3D stochastic model based on the deformation of an ellipsoid mesh according to multiple 3D random Gaussian fields, which allows fine modeling of details or textures, but is limited to star-shaped objects.
- GRAPE [28]: a 3D stochastic model based on hard sphere packing that uses objective functions to approximate as closely as possible the 2D morphological feature distributions that are targeted. Its main drawback, in the context of this study, is that the optimization of the parameters is subject to an a priori estimation of the object volumes, based on the assumption of cylindrical symmetry.

The optimal parameters of the three models are found by minimizing their respective cost functions using the PSO algorithm. The resulting 2D and 3D morphological feature distributions are shown in Figs. 13 and 14 for Exp. 1 and Exp. 2, respectively, and compared with the ground truth measured on the images in the case of 2D features.

5.2. 2D morphological characteristics

Visually, the VOX-STORM model appears to provide more consistent predictions than the other models in terms of 2D features, although the differences are minimal. The Total Variation Distance between each of the predictions and the ground truth, when known, is calculated and shown in Table 7, and VOX-STORM achieves better results in 75% of the cases. Overall, all three models are very successful in predicting the
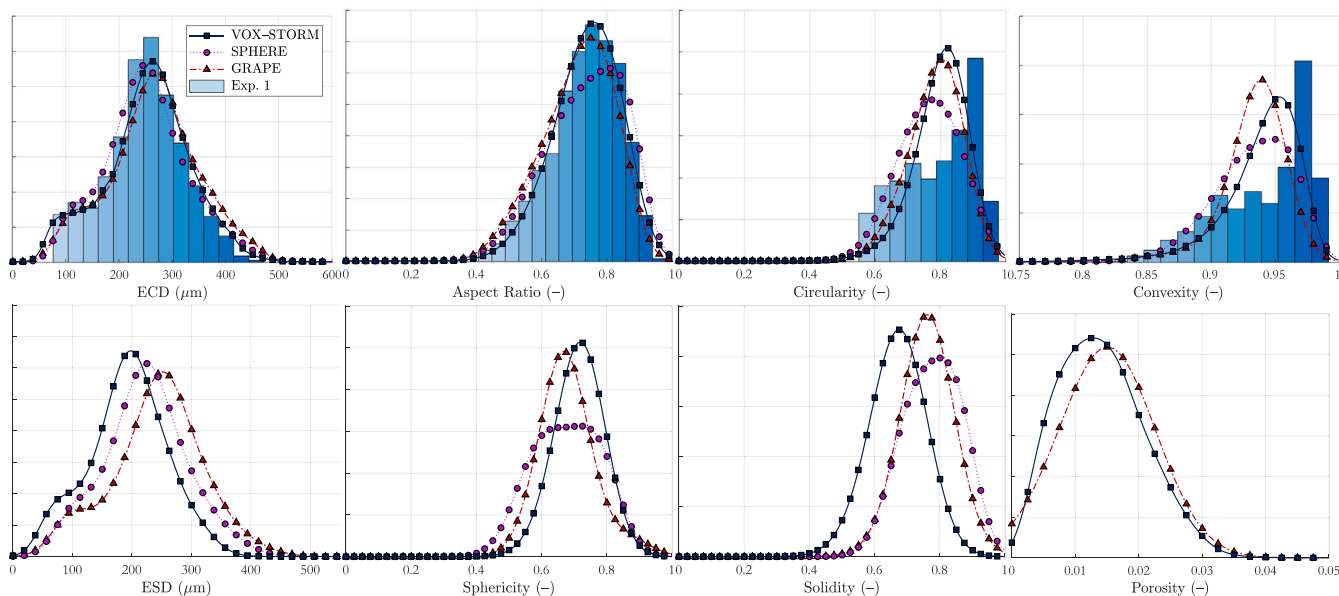
Fig. 13. Comparison of the predictions of 2D and 3D morphological features distributions of two stochastic geometrical models with those of the VOX-STORM model for Exp. 1. The distributions and histogram are expressed in terms of number density and are normalized.
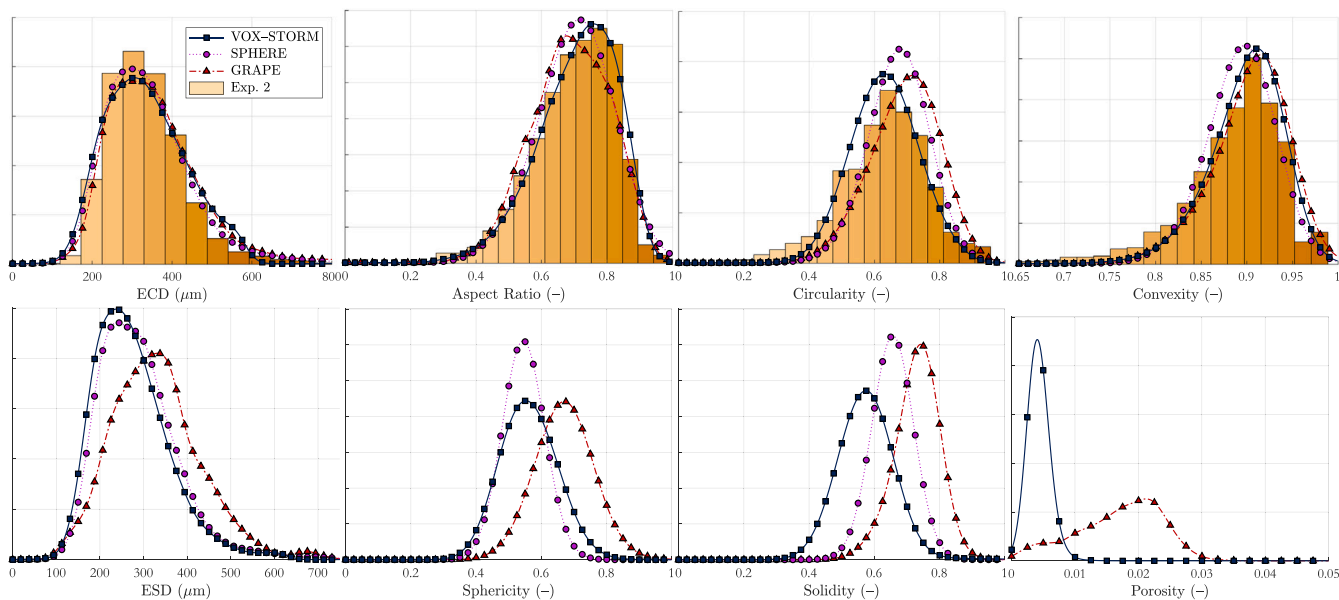

Fig. 14. Comparison of the predictions of 2D and 3D morphological features distributions of two stochastic geometrical models with those of the VOX-STORM model for Exp. 2. The distributions and histogram are expressed in terms of number density and are normalized.

2D morphological features of size and shape of the objects, i.e. the ECD and the AR.

The 2D characteristics of angularity and texture, namely the circularity and convexity, are predicted fairly well by all three models for Exp. 2, with a clear advantage for VOX-STORM for circularity. In contrast, the predictions for circularity and convexity in Exp. 1 are slightly less good, with the VOX-STORM model showing a small advantage for the convexity.

This difficulty in fitting all three models to the circularity and convexity distributions for Exp. 1, as opposed to Exp. 2, may be due to the fact that the object population in the images from Experiment 1 is more diverse, with many very compact and circular objects, as suggested by the two peaks close to 1 observed in Fig. 13 for circularity and convexity, and other much less compact objects, as suggested by both distributions and direct observations on images taken by the

morphogranulometer. In contrast, the population of objects from Exp. 2 would be more homogeneous and therefore easier for the models to simulate.

5.3. 3D morphological characteristics

Several observations can be made regarding the 3D morphological properties:

- In terms of size distributions, the VOX-STORM model performs much better than the other two models, as shown in Table 8, which compares the median ESD values predicted by the different models with a value measured by laser diffraction. Furthermore, the value obtained for Experiment 2 is identical to the value measured experimentally by Hamieh et al. [31].
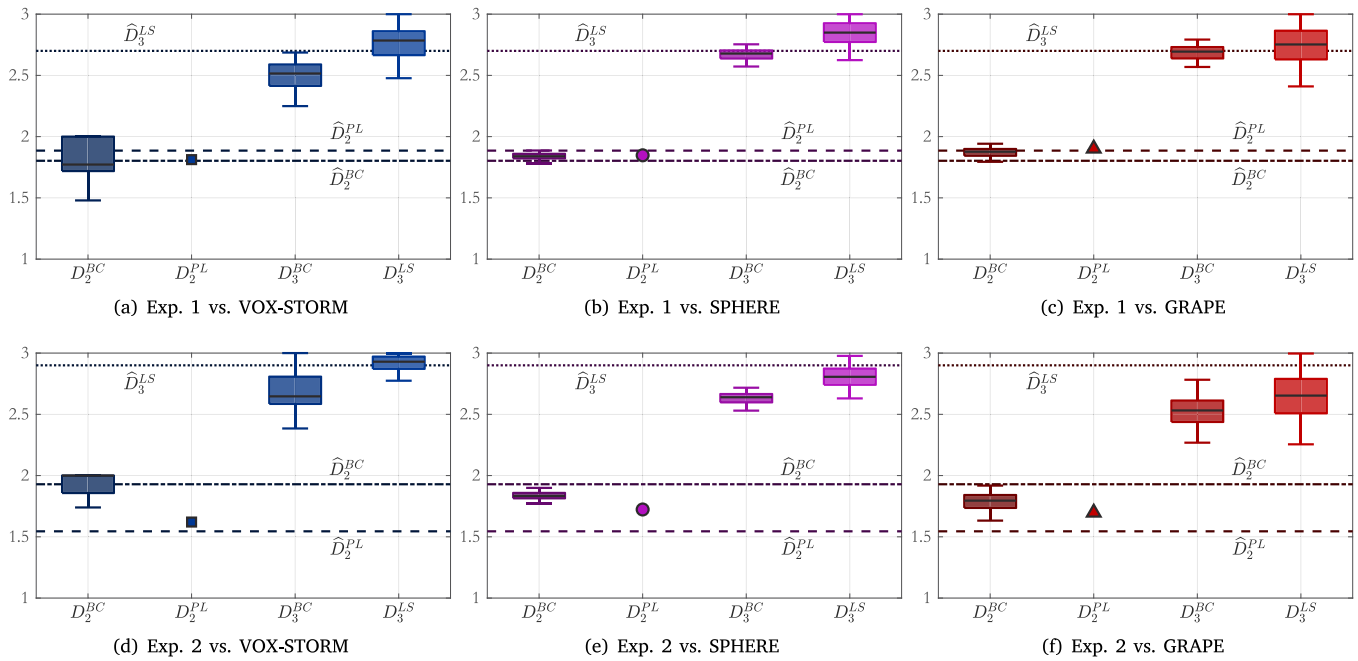
Fig. 15. Comparison of the predictions of the three different models for all 2D and 3D fractal dimensions for Exp. 1 and Exp. 2.

Table 7
Total Variation Distance between the distributions of 2D morphological features predicted by the three models considered (Fig. 13 and Fig. 14) and the ground truth obtained by analyzing the images acquired at the end of Exp. 1 and Exp. 2, respectively.

	Total Variation Distance – Exp. 1			
Models	ECD	AR	C	Co
VOX-STORM	**0.050**	**0.055**	**0.112**	**0.108**
SPHERE	0.055	0.064	0.129	0.119
GRAPE	0.087	0.076	0.121	0.198

	Total Variation Distance – Exp. 2			
Models	ECD	AR	C	Co
VOX-STORM	0.052	**0.036**	**0.132**	0.221
SPHERE	**0.032**	0.072	0.203	0.162
GRAPE	0.076	0.270	0.211	**0.158**

Table 8
Median value for ESD distributions predicted by the three models compared with a laser scattering measurement.

	ESD Median (μm)			
	Laser scattering	VOX-STORM	SPHERE	GRAPE
Exp. 1	165	**196**	223	248
Exp. 2	262	**262**	277	323

5.4. Fractal dimensions comparison

The lack of ground truth to measure model quality means that other methods and indicators must be used. For this reason, the calculation of 2D and 3D fractal dimensions can be an additional indicator of the predictive ability of the models. Therefore, the box-counting fractal dimensions (D_2^{BC} and D_3^{BC}), the fractal dimension defined by a power law relating the area of objects and a characteristic dimension (D_2^{PL}), and the mass fractal dimension (D_3^{LS}) – measured experimentally by laser scattering and by computer simulation for the model simulations – are calculated.

Fig. 15 and the results shown in Table 9 clearly show that the proposed model is much closer to the ground truth than the other two, with 2D fractal dimensions very close to those measured on images from the morphogranulometer, and 3D fractal dimensions obtained by laser diffraction simulation in agreement with experimental measurements, for both experiments. In contrast, the other two models obtained lower mass fractal dimensions for Exp. 2 than those predicted for Exp. 1, which contradicts the experimental measurements.

The mass fractal dimension D_3^{LS} is measured experimentally using a Mastersizer 3000 for the ground truth and simulated on the computer from voxelized object representations for synthetic objects. The scattering intensity $I(k)$ is given by the square modulus of the FFT_{3D} of the voxelized objects [39,58], and corrections based on Mie theory are applied to account for absorption and refraction [59], where the absorption and refractive indices of latex are 0.1 and 1.528, respectively. However, this is a simplified model based on assumptions that may not match the Mastersizer 3000 firmware in all respects. For this reason, there may not be direct equivalence between experimentally measured values of D_3^{LS} and those obtained by computer simulation.

- The fact that the SPHERE and VOX-STORM models often agree is a good sign. Since the GRAPE model relies on a priori volume estimation to predict 3D morphological features, its predictions should be treated with caution. In addition, the VOX-STORM model tends to generate objects of lower solidity. Beyond the predictive aspect, this is also a technical limitation of the other two models, which are not designed to generate objects with excessive concavity.

- Finally, the VOX-STORM model predicts a lower porosity for the objects in Exp. 2 (0.4% on average) than for those in Exp. 1 (1.3% on average). This is in agreement with experimental observations, where the objects in Exp. 2 are larger and more compact, probably due to the higher destabilization temperature, while the GRAPE model predicts the opposite, with the porosity of the objects in Exp. 2 (1.19% on average) almost identical to that in Exp. 1 (1.21% on average). The SHPERE model, on the other hand, only generates mesh and is not capable of predicting the porosity.

This makes it difficult to estimate the performance of different models in predicting 3D features. Nevertheless, VOX-STORM seems to obtain the most convincing results, with size statistics (ESD) closer to experimental measurements, and a more realistic prediction of porosity.

Table 9
Fractal dimensions (2D and 3D) predicted by the models and compared with the ground truth obtained by experimental measurement or image analysis. The average values in bold are the ones closest to the ground truth.

	Fractal dimensions			
	D_2^{BC}	D_2^{PL}	D_3^{BC}	D_3^{LS}
Exp. 1	1.80	1.89	–	2.7
VOX-STORM	**1.81**	1.81	2.54	**2.75**
SPHERE	1.84	1.85	2.67	2.85
GRAPE	1.86	**1.90**	2.66	2.75
	D_2^{BC}	D_2^{PL}	D_3^{BC}	D_3^{LS}
Exp. 2	1.93	1.55	–	2.9
VOX-STORM	**1.94**	**1.62**	2.76	**2.90**
SPHERE	1.83	1.72	2.62	2.81
GRAPE	1.78	1.70	2.52	2.64

Nevertheless, the qualitative interpretation of the results still makes sense, and the tendency of the VOX-STORM model to suggest a higher mass fractal dimension for Exp. 2 than for Exp. 1 is consistent with experimental measurements, contrary to the results predicted by the SPHERE model.

6. Discussion

The results obtained from experimental data and 3D printed aggregates indicate that the proposed model performs slightly better than the other two regarding 2D morphology. Similarly, in the case of 3D morphological features, laser diffraction measurements of size (ESD) and fractal dimension (D_3^{LS}) confirm that VOX-STORM still outperforms the other two. It should be noted that all morphological properties (except the various fractal dimensions) are computed using built-in MATLAB® functions (`alphaShape`, `convhull`, `convhulln`, `regionprops3`), which in particular provide a set of tools for performing measurements directly on alpha shapes.

The advantages of the VOX-STORM model can be summarized as follows

1. Better fitting and predictive performance for 2D and 3D morphological features than other stochastic geometrical models based on hard sphere packing or mesh generation.
2. The ability to model non-compact (i.e., porous), non-convex, non-star-shaped objects, and the ability to provide information about object porosity.
3. Fast generation of large numbers of objects with complex geometries, as well as fast calculation of their morphological properties (Fig. 16).
4. A high degree of flexibility thanks to the large number of parameters that allow the model to generate objects with a wide variety of morphological characteristics.
5. Voxel-mesh duality for realistic rendering, ideal for building databases for machine learning and/or deep learning applications.

In terms of time to generate objects and time required to measure morphological features on them, Fig. 16 shows a benchmark of the three models used in the previous section. It can be seen that although the VOX-STORM model is not as fast as a stochastic model based on the deformation of an ellipsoid mesh, it still far outperforms all other models in terms of computation time for measuring morphological features. This is because morphological features are measured based on the mesh defined by the alpha shape. Because of the way this mesh is generated, it can be seen as an adaptive form of a mesh, where each surface element does not have the same size, unlike the SPHERE model. Because the cell size for an alpha shape is variable, the number of vertices is reduced and computation time is minimized.
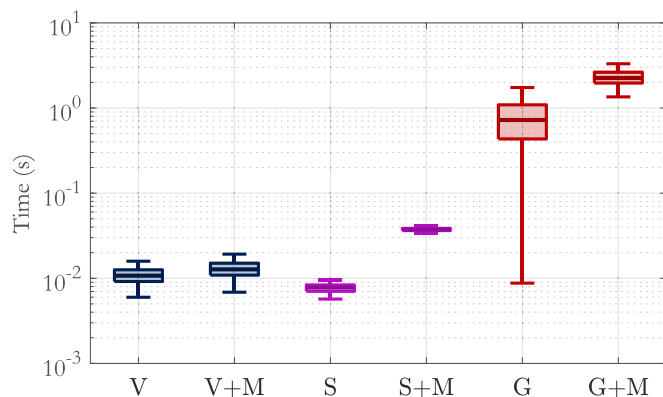

Fig. 16. Computational time required for each model to generate objects and perform morphological measurements. The data correspond to a total of 20,000 objects, divided into two sets of 10,000 elements for each of the parameterizations corresponding to the two experiments. The letters V, S, and G correspond to the VOX-STORM, SPHERE, and GRAPE models, respectively, and the suffix + M indicates that the time taken to measure morphological features is added.

It is noteworthy that the variance of the generation and measurement times for the SPHERE model, which is based on a single mesh, is extremely small and does not depend at all on the size of the objects modeled, unlike the other two approaches, where the number of elementary particles (voxels or hard spheres) increases with the object size and has a significant influence on the generation and measurement times.

Finally, the GRAPE model, based on hard sphere packing, offers the worst performance in terms of computational time, which varies considerably with object size, as can be clearly seen from the large variance visible in the box plot in Fig. 16. The time required for 3D measurements is also much greater than for the other two approaches, for which a mesh of the outer surface is provided directly as output.

However, the VOX-STORM model has the following limitations

1. The proposed model proved to be very effective in modeling the population of Exp. 2, both at the 2D and 3D levels. Nevertheless, the modeling of Exp. 1 is less satisfactory for angularity and texture features, although size (ECD) and shape (AR, fractal dimensions) features are quite well approximated. As mentioned in the previous section, this may be due to the fact that the population of latex aggregates present in Exp. 1 is more heterogeneous than in Exp. 2. One solution could be to use random variables, possibly correlated, instead of fixed scalars in the parameterization of the model, as is already the case for the number of iterations.
2. As with any iterative model, the computation time increases with the number of iterations and the size of the objects. However, the time complexity is polynomial due to the convolution-based 3D voxel grid generation and the fact that the alpha shapes are derived from a Delaunay triangulation whose worst-case complexity is $\mathcal{O}(n \log n)$ [60], where n is the number of voxels, unlike hard sphere packing models whose complexity is much higher and sometimes exponential [61].
3. The flexibility of VOX-STORM is partly due to its 8 parameters (7 for the optimization process). However, this means that finding an optimal parameter set to fit a new population of objects from 2D images using an optimization process is much more time consuming and difficult than for models with fewer parameters. For comparison, the SPHERE model requires 5 parameters during the optimization process, and the GRAPE model requires only 2 (sphere size and overlap parameters), but with strong assumptions about object geometry.

Despite these limitations, the proposed model overall performed better than other approaches for modeling two populations of aggregates and predicting their 3D morphological properties from projected 2D images. Among the improvements mentioned are a finer parameterization of the convolution kernel and the use of random variables as parameters, especially for the intensity, the correlation lengths of the Gaussian fields, and the α parameter, although these approaches would significantly increase the already large number of parameters.

The direct continuation of this work will consist mainly in applying the proposed method to in-situ images (such as the one shown in Fig. 9(a)), where no assumption about the orientation of the objects is required, which is a necessary condition for the implementation of the other two models tested and constitutes one of their main limitations.

Another prospect is to use the ability of the VOX-STORM model to generate photorealistic objects (Fig. 9(b)) to train deep learning models to predict the 2D and 3D morphological feature distributions of objects directly from in-situ images, in an approach similar to that recently developed by Dia et al. [62].

7. Conclusion

This paper proposes a model and a method for predicting the 3D morphological characteristics of latex aggregates from measurements of 2D morphological characteristics made on projected images. The proposed model, called VOX-STORM, is based on the use of a dual paradigm: the rapid generation of a voxelized structure of the objects by successive convolution, and the description of the surface of the objects in the form of a mesh obtained by computing an alpha shape. The model is made flexible by parameterizing the convolution kernel and by using two random Gaussian fields to modify the probability of activation of a boundary voxel at each iteration.

To match the morphological feature distributions of the objects generated by the model with those measured by image analysis, a cost function is defined and minimized by Particle Swarm Optimization. The method is first validated by considering a population of 3D printed aggregates imaged by a morphogranulometer. Relative errors on the mean values of 2D and 3D features were all below 2.5%, and below 1% for 2D features. A second numerical validation was performed on a population of 40,000 synthetic objects generated by the VOX-STORM model itself, and the results were again conclusive, quantified by Total Variation Distance calculations.

Then, the method is applied to two series of 3500 images taken by a morphogranulometer, each from two experiments designed to study the formation of MBS latex aggregates under different conditions. Two other stochastic geometrical models, one based on hard sphere packing and the other on random mesh deformation, are also used to evaluate the performance of the proposed model.

The results obtained are compared with those of the other models and with experimental laser diffraction measurements for the mass fractal dimension and ESD. In virtually all scenarios, the proposed model outperforms the other two, both in terms of accuracy and speed, and is always in agreement with experimental observations. These encouraging results demonstrate the flexibility of the model and its ability to rapidly generate a large number of objects with very different morphological characteristics, which could find numerous applications in chemical or materials engineering. Furthermore, although only images from a morphogranulometer were used in this study, the method can be applied to any type of image, regardless of the size or shape distribution of the objects, and at any scale.

Finally, in the last section, the advantages and limitations of the proposed model are discussed and avenues for improvement are suggested, as well as prospects for future work, including application of the method to in-situ images and comparison with deep learning-based techniques.

Additional resources

The MATLAB® (2023b) code for the VOX-STORM model is available in a GitHub repository at: https://github.com/ltheodon/VOX-STORM.

The STL files used to design the 3D printed aggregates are available for purchase on CGTrader at: https://www.cgtrader.com/3d-models/food/fruit/blackberry-001.

CRediT authorship contribution statement

L. Théodon: Writing – review & editing, Writing – original draft, Visualization, Validation, Software, Methodology, Investigation, Conceptualization. **J. Debayle:** Writing – review & editing, Supervision. **C. Coufort-Saudejaud:** Writing – review & editing, Supervision.

Declaration of competing interest

The authors declare that they have no known competing financial interests or personal relationships that could have appeared to influence the work reported in this paper.

Data availability

The authors do not have permission to share data.

Acknowledgments

Appendix A. Supplementary data

Supplementary material related to this article can be found online at https://doi.org/10.1016/j.powtec.2024.119983.

References

[1] E.M. Alander, M.S. Uusi-Penttilä, Å.C. Rasmuson, Characterization of paracetamol agglomerates by image analysis and strength measurement, Powder Technol. 130 (1) (2003) 298–306, http://dx.doi.org/10.1016/S0032-5910(02)00208-5.

[2] G.A. Kelesidis, S.E. Pratsinis, Determination of the volume fraction of soot accounting for its composition and morphology, Proc. Combust. Inst. 38 (1) (2021) 1189–1196, http://dx.doi.org/10.1016/j.proci.2020.07.055, URL https://www.sciencedirect.com/science/article/pii/S1540748920304879.

[3] C. Turchiuli, E. Castillo-Castaneda, Agglomerates structure characterization using 3D-image reconstruction, Part. Part. Syst. Charact. 26 (1–2) (2009) 25–33, http://dx.doi.org/10.1002/ppsc.200700028.

[4] N. Faria, M. Pons, S. Feyo de Azevedo, F. Rocha, H. Vivier, Quantification of the morphology of sucrose crystals by image analysis, Powder Technol. 133 (1) (2003) 54–67, http://dx.doi.org/10.1016/S0032-5910(03)00078-0.

[5] C. Jin, F. Zou, X. Yang, Z. You, 3D quantification for aggregate morphology using surface discretization based on solid modeling, J. Mater. Civ. Eng. 31 (7) (2019) 04019123, http://dx.doi.org/10.1061/(ASCE)MT.1943-5533.0002766.

[6] P. Monchot, L. Coquelin, K. Guerroudj, N. Feltin, A. Delvallée, L. Crouzier, N. Fischer, Deep learning based instance segmentation of titanium dioxide particles in the form of agglomerates in scanning electron microscopy, Nanomaterials 11 (4) (2021) http://dx.doi.org/10.3390/nano11040968, URL https://www.mdpi.com/2079-4991/11/4/968.

[7] R. Pashminehazar, S.J. Ahmed, A. Kharaghani, E. Tsotsas, Spatial morphology of maltodextrin agglomerates from X-ray microtomographic data: Real structure evaluation vs. spherical primary particle model, Powder Technol. 331 (2018) 204–217, http://dx.doi.org/10.1016/j.powtec.2018.03.008, URL https://www.sciencedirect.com/science/article/pii/S0032591018301918.

[8] P. Liu, J. Hu, D. Wang, M. Oeser, S. Alber, W. Ressel, G. Canon Falla, Modelling and evaluation of aggregate morphology on asphalt compression behavior, Constr. Build. Mater. 133 (2017) 196–208, http://dx.doi.org/10.1016/j.conbuildmat.2016.12.041, URL https://www.sciencedirect.com/science/article/pii/S095006181631947X.

[9] P. Wang, N. Gao, K. Ji, L. Stewart, C. Arson, DEM analysis on the role of aggregates on concrete strength, Comput. Geotech. 119 (2020) 103290, http://dx.doi.org/10.1016/j.compgeo.2019.103290, URL https://www.sciencedirect.com/science/article/pii/S0266352X19303544.

[10] L. Guérin, C. Frances, A. Liné, C. Coufort-Saudejaud, Fractal dimensions and morphological characteristics of aggregates formed in different physico-chemical and mechanical flocculation environments, Colloids Surf. A 560 (2019) 213–222, http://dx.doi.org/10.1016/j.colsurfa.2018.10.017, URL https://www.sciencedirect.com/science/article/pii/S0927775718313153.

[11] C. Bower, C. Washington, T. Purewal, The use of image analysis to characterize aggregates in a shear field, Colloids Surf. A 127 (1) (1997) 105–112, http://dx.doi.org/10.1016/S0927-7757(96)03945-3, URL https://www.sciencedirect.com/science/article/pii/S0927775796039453.

[12] S. Tang, C.M. McFarlane, G.C. Paul, C.R. Thomas, Characterising latex particles and fractal aggregates using image analysis, Colloid Polym. Sci. 277 (4) (1999) 325–333, http://dx.doi.org/10.1007/s003960050388.

[13] Y. Lin, Z.-Y. Yin, X. Wang, L. Huang, A systematic 3D simulation method for geomaterials with block inclusions from image recognition to fracturing modelling, Theor. Appl. Fract. Mech. 117 (2022) 103194, http://dx.doi.org/10.1016/j.tafmec.2021.103194, URL https://www.sciencedirect.com/science/article/pii/S0167844221002913.

[14] Y. Lin, J. Ma, Z. Lai, L. Huang, M. Lei, A FDEM approach to study mechanical and fracturing responses of geo-materials with high inclusion contents using a novel reconstruction strategy, Eng. Fract. Mech. 282 (2023) 109171, http://dx.doi.org/10.1016/j.engfracmech.2023.109171, URL https://www.sciencedirect.com/science/article/pii/S0013794423001297.

[15] Y. Lin, Z. Lai, J. Ma, L. Huang, A combined weighted Voronoi tessellation and random field approach for modeling heterogeneous rocks with correlated grain structure, Constr. Build. Mater. 416 (2024) 135228, http://dx.doi.org/10.1016/j.conbuildmat.2024.135228, URL https://www.sciencedirect.com/science/article/pii/S0950061824003696.

[16] R.I. Jeldres, P.D. Fawell, B.J. Florio, Population balance modelling to describe the particle aggregation process: A review, Powder Technol. 326 (2018) 190–207, http://dx.doi.org/10.1016/j.powtec.2017.12.033, URL https://www.sciencedirect.com/science/article/pii/S003259101730983X.

[17] S. Bhoi, S.R. Kolan, A. Bück, E. Tsotsas, Population balance modeling of formation and breakage of nanoparticle agglomerates in a spouted bed, Powder Technol. 433 (2024) 119271, http://dx.doi.org/10.1016/j.powtec.2023.119271, URL https://www.sciencedirect.com/science/article/pii/S0032591023010549.

[18] L. Théodon, J. Debayle, C. Coufort-Saudejaud, Morphological characterization of aggregates and agglomerates by image analysis: A systematic literature review, Powder Technol. 430 (2023) 119033, http://dx.doi.org/10.1016/j.powtec.2023.119033, URL https://www.sciencedirect.com/science/article/pii/S0032591023008161.

[19] A. Mehle, B. Likar, D. Tomaževič, In-line recognition of agglomerated pharmaceutical pellets with density-based clustering and convolutional neural network, in: 2017 Fifteenth IAPR International Conference on Machine Vision Applications, MVA, 2017, pp. 9–12, http://dx.doi.org/10.23919/MVA.2017.7986760.

[20] M. Frei, F. Kruis, Image-based size analysis of agglomerated and partially sintered particles via convolutional neural networks, Powder Technol. 360 (2020) 324–336, http://dx.doi.org/10.1016/j.powtec.2019.10.020, URL https://www.sciencedirect.com/science/article/pii/S003259101930854X.

[21] B. Rühle, J.F. Krumrey, V.-D. Hodoroaba, Workflow towards automated segmentation of agglomerated, non-spherical particles from electron microscopy images using artificial neural networks, Sci. Rep. 11 (1) (2021) 4942, http://dx.doi.org/10.1038/s41598-021-84287-6.

[22] K. Giannis, C. Thon, G. Yang, A. Kwade, C. Schilde, Predicting 3D particles shapes based on 2D images by using convolutional neural network, Powder Technol. 432 (2024) 119122, http://dx.doi.org/10.1016/j.powtec.2023.119122, URL https://www.sciencedirect.com/science/article/pii/S0032591023009051.

[23] L. Wang, W. Sun, E. Tutumluer, C. Druta, Evaluation of aggregate imaging techniques for quantification of morphological characteristics, Transp. Res. Rec. 2335 (1) (2013) 39–49, http://dx.doi.org/10.3141/2335-05.

[24] M. de Langlard, F. Lamadie, S. Charton, J. Debayle, Estimation of 3D geometrical properties of spheroid-like particle systems using projection images, in: 2020 10th International Symposium on Signal, Image, Video and Communications, ISIVC, 2021, pp. 1–6, http://dx.doi.org/10.1109/ISIVC49222.2021.9487552.

[25] M. Moreaud, J. Chaniot, T. Fournel, J.M. Becker, L. Sorbier, Multi-scale stochastic morphological models for 3D complex microstructures, in: 2018 17th Workshop on Information Optics, WIO, 2018, pp. 1–3, http://dx.doi.org/10.1109/WIO.2018.8643455.

[26] M. Moreaud, G. Ferri, S. Humbert, M. Digne, J.-M. Schweitzer, Simulation of large aggregate particles system with a new morphological model, Image Anal. Stereol. 40 (2) (2021) 71–84, http://dx.doi.org/10.5566/ias.2488, URL https://www.ias-iss.org/ojs/IAS/article/view/2488.

[27] O.V. Tomchuk, M.V. Avdeev, L.A. Bulavin, Modeling fractal aggregates of polydisperse particles with tunable dimension, Colloids Surf. A 605 (2020) 125331, http://dx.doi.org/10.1016/j.colsurfa.2020.125331, URL https://www.sciencedirect.com/science/article/pii/S0927775720309249.

[28] L. Théodon, C. Coufort-Saudejaud, J. Debayle, GRAPE: A stochastic geometrical 3D model for aggregates of particles with tunable 2D morphological projected properties, Image Anal. Stereol. 42 (1) (2023) 1–16, http://dx.doi.org/10.5566/ias.2875, URL https://www.ias-iss.org/ojs/IAS/article/view/2875.

[29] L. Théodon, C. Coufort-Saudejaud, J. Debayle, A stochastic model based on Gaussian random fields to characterize the morphology of granular objects, Pattern Recognit. 149 (2024) 110255, http://dx.doi.org/10.1016/j.patcog.2024.110255, URL https://www.sciencedirect.com/science/article/pii/S0031320324000062.

[30] H. Edelsbrunner, D. Kirkpatrick, R. Seidel, On the shape of a set of points in the plane, IEEE Trans. Inform. Theory 29 (4) (1983) 551–559, http://dx.doi.org/10.1109/TIT.1983.1056714.

[31] A. Hamieh, C. Coufort-Saudejaud, A. Couffin, A. Liné, C. Frances, Temperature influence on MBS latex aggregate morphology, Colloids Surf. A 676 (2023) 132139, http://dx.doi.org/10.1016/j.colsurfa.2023.132139, URL https://www.sciencedirect.com/science/article/pii/S0927775723012232.

[32] C. Navarro, S. Girois, E. Bay, J.-C. Saint-Martin, Process for core-shell impact modifiers and impact modified thermoplastic composition with enhanced hydrolytic resistance, 2012, Patent SG182095A1. July 30, 2012.

[33] K. Falconer, Hausdorff measure and dimension, in: Fractal Geometry, John Wiley & Sons, Ltd, 2003, pp. 27–38, http://dx.doi.org/10.1002/0470013850.ch2, arXiv:https://onlinelibrary.wiley.com/doi/pdf/10.1002/0470013850.ch2 URL https://onlinelibrary.wiley.com/doi/abs/10.1002/0470013850.ch2.

[34] L. Guérin, C. Coufort-Saudejaud, A. Liné, C. Frances, Dynamics of aggregate size and shape properties under sequenced flocculation in a turbulent Taylor-Couette reactor, J. Colloid Interface Sci. 491 (2017) 167–178, http://dx.doi.org/10.1016/j.jcis.2016.12.042, URL https://www.sciencedirect.com/science/article/pii/S0021979716310426.

[35] Z. Kulpa, Area and perimeter measurement of blobs in discrete binary pictures, Comput. Graph. Image Process. 6 (5) (1977) 434–451, http://dx.doi.org/10.1016/S0146-664X(77)80021-X, URL https://www.sciencedirect.com/science/article/pii/S0146664X7780021X.

[36] E. Pirard, G. Dislaire, Robustness of planar shape descriptors of particles, in: Proceedings Mathematical Geology Congress, 2005.

[37] B.J. Florio, P.D. Fawell, M. Small, The use of the perimeter-area method to calculate the fractal dimension of aggregates, Powder Technol. 343 (2019) 551–559, http://dx.doi.org/10.1016/j.powtec.2018.11.030, URL https://www.sciencedirect.com/science/article/pii/S0032591018309343.

[38] M. Soos, L. Ehrl, M.U. Bäbler, M. Morbidelli, Aggregate breakup in a contracting nozzle, Langmuir 26 (1) (2010) 10–18, http://dx.doi.org/10.1021/la903982n.

[39] C.M. Sorensen, Light scattering by fractal aggregates: A review, Aerosol Sci. Technol. 35 (2) (2001) 648–687, http://dx.doi.org/10.1080/02786820117868, arXiv:https://www.tandfonline.com/doi/pdf/10.1080/02786820117868 URL https://www.tandfonline.com/doi/abs/10.1080/02786820117868.

[40] P. Adler, C. Jacquin, J. Quiblier, Flow in simulated porous media, Int. J. Multiph. Flow 16 (5) (1990) 691–712, http://dx.doi.org/10.1016/0301-9322(90)90025-E, URL https://www.sciencedirect.com/science/article/pii/030193229090025E.

[41] Z. Liang, C. Fernandes, F. Magnani, P. Philippi, A reconstruction technique for three-dimensional porous media using image analysis and Fourier transforms, J. Pet. Sci. Eng. 21 (3) (1998) 273–283, http://dx.doi.org/10.1016/S0920-4105(98)00077-1, URL https://www.sciencedirect.com/science/article/pii/S0920410598000771.

[42] A. Lang, J. Potthoff, Fast simulation of Gaussian random fields, 17 (3) (2011) 195–214, http://dx.doi.org/10.1515/mcma.2011.009.

[43] P. Soille, Morphological Image Analysis: Principles and Applications, Springer Berlin Heidelberg, 2013, URL https://books.google.fr/books?id=ZFzxCAAAQBAJ.

[44] J. Karch, Improving on adjusted R-squared, Collabra: Psychology 6 (1) (2020) 45, http://dx.doi.org/10.1525/collabra.343, arXiv:https://online.ucpress.edu/collabra/article-pdf/6/1/45/483406/343-4856-1-pb.pdf.

[45] D. Wei, J. Wang, B. Zhao, A simple method for particle shape generation with spherical harmonics, Powder Technol. 330 (2018) 284–291, http://dx.doi.org/10.1016/j.powtec.2018.02.006, URL https://www.sciencedirect.com/science/article/pii/S0032591018301189.

[46] X. Wei, Y. Sun, J. Ouyang, H. Gong, J. Chen, Surface subdivision-based method for modeling three-dimensional aggregate with controllable concavity and texture in asphalt concrete mesostructure, Powder Technol. 434 (2024) 119311, http://dx.doi.org/10.1016/j.powtec.2023.119311, URL https://www.sciencedirect.com/science/article/pii/S003259102301094X.

[47] L. Zhang, H. Wang, Z. Ren, Computational analysis of thermal conductivity of asphalt mixture using virtually generated three-dimensional microstructure, J. Mater. Civ. Eng. 29 (12) (2017) 04017234, http://dx.doi.org/10.1061/(ASCE)MT.1943-5533.0002081, arXiv:https://ascelibrary.org/doi/10.1061/(ASCE)MT.1943-5533.0002081 URL https://ascelibrary.org/doi/10.1061/(ASCE)MT.1943-5533.0002081.

[48] J. Zhang, Z. Wang, H. Yang, Z. Wang, X. Shu, 3D meso-scale modeling of reinforcement concrete with high volume fraction of randomly distributed aggregates, Constr. Build. Mater. 164 (2018) 350–361, http://dx.doi.org/10.1016/j.conbuildmat.2017.12.229, URL https://www.sciencedirect.com/science/article/pii/S0950061817326351.

[49] M. Wozniak, F. Onofri, S. Barbosa, J. Yon, J. Mroczka, Comparison of methods to derive morphological parameters of multi-fractal samples of particle aggregates from TEM images, J. Aerosol Sci. 47 (2012) 12–26, http://dx.doi.org/10.1016/j.jaerosci.2011.12.008, URL https://www.sciencedirect.com/science/article/pii/S0021850211001984.

[50] M. Moreaud, G. Ferri, S. Humbert, M. Digne, J.-M. Schweitzer, Simulation of large aggregate particles system with a new morphological model, Image Anal. Stereol. 40 (2) (2021) 71–84, http://dx.doi.org/10.5566/ias.2488, URL https://www.ias-iss.org/ojs/IAS/article/view/2488.

[51] G. Mollon, J. Zhao, Generating realistic 3D sand particles using Fourier descriptors, Granul. Matter 15 (1) (2013) 95–108, http://dx.doi.org/10.1007/s10035-012-0380-x.

[52] G. Mollon, J. Zhao, 3D generation of realistic granular samples based on random fields theory and Fourier shape descriptors, Comput. Methods Appl. Mech. Engrg. 279 (2014) 46–65, http://dx.doi.org/10.1016/j.cma.2014.06.022, URL https://www.sciencedirect.com/science/article/pii/S0045782514002084.

[53] H. Moussaoui, J. Laurencin, Y. Gavet, G. Delette, M. Hubert, P. Cloetens, T. Le Bihan, J. Debayle, Stochastic geometrical modeling of solid oxide cells electrodes validated on 3D reconstructions, Comput. Mater. Sci. 143 (2018) 262–276, http://dx.doi.org/10.1016/j.commatsci.2017.11.015, URL https://www.sciencedirect.com/science/article/pii/S0927025617306432.

[54] L. Takács, - On the comparison of theoretical and empirical distribution functions, in: B. Szyszkowicz (Ed.), Asymptotic Methods in Probability and Statistics, North-Holland, Amsterdam, 1998, pp. 213–231, http://dx.doi.org/10.1016/B978-044450083-0/50014-9, URL https://www.sciencedirect.com/science/article/pii/B9780444500830500149.

[55] J. Kennedy, R. Eberhart, Particle swarm optimization, in: Proceedings of ICNN'95 - International Conference on Neural Networks, Vol. 4, 1995, pp. 1942–1948, http://dx.doi.org/10.1109/ICNN.1995.488968.

[56] L. Théodon, C. Coufort-Saudejaud, A. Hamieh, J. Debayle, Morphological characterization of compact aggregates using image analysis and a geometrical stochastic 3D model, in: 2023 IEEE 13th International Conference on Pattern Recognition Systems, ICPRS, 2023, pp. 1–7, http://dx.doi.org/10.1109/ICPRS58416.2023.10179036.

[57] A.B. Tsybakov, Introduction to Nonparametric Estimation, first ed., Springer Publishing Company, Incorporated, 2008.

[58] K.P. Dao, K. Lee, Y. Hong, S. Shin, S. Lee, D.S. Hwang, Y. Park, 3D Fourier transformation light scattering for reconstructing extend angled resolved light scattering of individual particles, 2021, URL https://api.semanticscholar.org/CorpusID:231846707.

[59] P.W. Barber, S.C. Hill, Light Scattering by Particles: Computational Methods, World Scientific, 1990, http://dx.doi.org/10.1142/0784, arXiv:https://www.worldscientific.com/doi/pdf/10.1142/0784 URL https://www.worldscientific.com/doi/abs/10.1142/0784.

[60] G. Leach, Improving worst-case optimal delaunay triangulation algorithms, 1992, URL https://api.semanticscholar.org/CorpusID:18356714.

[61] E. Lozano, D. Roehl, W. Celes, M. Gattass, An efficient algorithm to generate random sphere packs in arbitrary domains, Comput. Math. Appl. 71 (8) (2016) 1586–1601, http://dx.doi.org/10.1016/j.camwa.2016.02.032, URL https://www.sciencedirect.com/science/article/pii/S0898122116300864.

[62] K. Dia, F. Lamadie, J. Debayle, Retrieving mean volumetric properties of multiphase flows from 2D images: A new approach combining deep learning algorithms and 3D modelling, Chem. Eng. Sci. 279 (2023) 118933, http://dx.doi.org/10.1016/j.ces.2023.118933, URL https://www.sciencedirect.com/science/article/pii/S000925092300489X.